Physical Sciences/Earth, Atmospheric, and Planetary Sciences

Asynchronous warming and $\delta^{18}O$ evolution of deep Atlantic water masses during the last deglaciation

(Short title: Asynchronous deglacial warming of the deep Atlantic)

Jiaxu Zhang[a,1,2], Zhengyu Liu[a], Esther C. Brady[b], Delia W. Oppo[c], Peter U. Clark[d], Alexandra Jahn[e], Shaun A. Marcott[f] & Keith Lindsay[b]

[a]Center for Climatic Research and Department of Atmospheric and Oceanic Sciences, University of Wisconsin-Madison, Madison, WI 53706;
[b]Climate and Global Dynamics Division, National Center for Atmospheric Research, Boulder, CO 80307;
[c]Department of Geology and Geophysics, Woods Hole Oceanographic Institution, Woods Hole, MA 02543;
[d]College of Earth, Ocean, and Atmospheric Sciences, Oregon State University, Corvallis, OR 97331;
[e]Department of Atmospheric and Oceanic Sciences and the Institute of Arctic and Alpine Research, University of Colorado Boulder, Boulder, CO 80309;
[f]Department of Geoscience, University of Wisconsin-Madison, Madison, WI 53706

[1] Present address: CCS-2 and T-3/CNLS, Los Alamos National Laboratory, Los Alamos, NM 87545.

[2] Corresponding author: Jiaxu Zhang, Los Alamos National Laboratory, MS B258, Los Alamos, NM 87545. Tel: (505)665-4698. E-mail: jiaxu@lanl.gov

Keywords: Atlantic water masses, last deglaciation, oxygen isotopes, deep ocean warming.

Abstract

The large-scale reorganization of deep-ocean circulation in the Atlantic involving changes in North Atlantic Deep Water (NADW) and Antarctic Bottom Water (AABW) played a critical role in regulating hemispheric and global climate during the last deglaciation. However, changes in the relative contributions of NADW and AABW and their properties are poorly constrained by marine records, including $\delta^{18}O$ of benthic foraminiferal calcite ($\delta^{18}O_c$). Here we use an isotope-enabled ocean general circulation model with realistic geometry and forcing conditions to simulate the deglacial water mass and $\delta^{18}O$ evolution. Model results suggest that in response to North Atlantic freshwater forcing during the early phase of the last deglaciation, NADW nearly collapses while AABW mildly weakens. Rather than reflecting changes in NADW or AABW properties due to freshwater input as suggested previously, the observed phasing difference of deep $\delta^{18}O_c$ likely reflects early warming of the deep northern North Atlantic by ~1.4°C while deep Southern Ocean temperature remains largely unchanged. We propose a thermodynamic mechanism to explain the early warming in the North Atlantic, featuring a strong mid-depth warming and enhanced downward heat flux via vertical mixing. Our results emphasize that the way ocean circulation affects heat, a dynamic tracer, is considerably different than how it affects passive tracers like $\delta^{18}O$, and call for caution when inferring water mass changes from $\delta^{18}O_c$ records while assuming uniform changes in deep temperatures.

Significance Statement

The reorganizations of deep Atlantic water masses are widely thought to regulate glacial-interglacial climate changes. However, the pattern of reorganizations and their impact on ocean tracer transport remains poorly constrained by marine proxies. Our modeling study, which simulates the coevolution of water masses and oxygen isotopes during the last deglaciation, suggests that deglacial meltwater input causes both northern- and southern-sourced deepwater transports to decrease. This reorganization pattern leads to asynchronous warming between the deep North and South Atlantic, which might have caused the observed deglacial phasing difference in deepwater oxygen isotope records between these ocean basins. We further propose a new mechanism to explain the early warming in the northern North Atlantic.

\body

A number of marine records provide evidence for major reorganizations of ocean circulation during the last deglaciation, especially changes in formation and transport of North Atlantic Deep Water (NADW) and Antarctic Bottom Water (AABW) (1, 2). Such deepwater mass changes were particularly pronounced during Heinrich Stadial 1 (HS1; 17.5–14.7 ka), when a significantly reduced Atlantic Meridional Overturning Circulation (AMOC) (3) led to a strong cooling in the Northern Hemisphere coupled with a warming in the Southern Hemisphere. However, the relative contribution of NADW and AABW to changes in deep circulation and its impact on tracer transport is poorly constrained during HS1, which limits our understanding of crucial ocean thermodynamic and dynamic processes that drive heat and freshwater transport as well as the carbon cycle and ultimately affect global climate (4, 5).

In addition to nutrient proxies such as $\delta^{13}C$ and Cd/Ca, and kinematic tracers such as $^{231}Pa/^{230}Th$, high-resolution deep-sea benthic foraminiferal calcite ($\delta^{18}O_c$) records have also been commonly used to infer water mass changes (6–10). $\delta^{18}O_c$ changes are well understood to reflect the combined influence of variations in deepwater temperature and the oxygen isotopic composition of the water ($\delta^{18}O_w$). One notable feature of these $\delta^{18}O_c$ records below 3000 m is the decrease in $\delta^{18}O_c$ at the start of HS1 in the northern North Atlantic relative to that in the Southern Ocean (8). The cause of this phasing difference and its implication for abyssal water masses remains unclear, however, because of the difficulty of separating the effects of water temperature and $\delta^{18}O_w$ on the $\delta^{18}O_c$ signal. Some studies suggest that this phasing reflects changes in the deep-ocean circulation pattern, namely a northward expansion of southern-sourced ^{18}O-depleted deepwater in response to a reduced AMOC (6, 7). In contrast, others conclude that this phasing reflects changes in the isotopic composition of source waters, with northern-sourced ^{18}O-depleted

76 waters continuing to fill much of the intermediate and deep Atlantic with a moderately reduced
77 AMOC (8–10). Assessing the potential contribution of temperature to the $\delta^{18}O_c$ records requires
78 the development of high-resolution temperature reconstructions (e.g., Mg/Ca) to isolate the $\delta^{18}O_w$
79 signal, but this has proven to be difficult for intermediate and deep-ocean water masses (11). Here
80 we provide an independent means to evaluate this issue by using an isotope-enabled ocean general
81 circulation model that simulates changes in both water-mass temperature and $\delta^{18}O_w$ in response to
82 changes in ocean circulation during the last deglaciation.
83
84 **Isotope-enabled, Transient Ocean Simulation**
85
86 Numerous modeling studies have explored possible forcing mechanisms involved in the deglacial
87 evolution of the ocean (12–17). One challenge faced by these models is in comparing and
88 validating their results directly against proxy records, either because the models do not simulate
89 the same geo-tracers estimated by proxies, or because those models that simulate proxy-related
90 geo-tracers are forced by idealized climate forcing (e.g., idealized freshwater perturbations for a
91 few hundred years). We address this challenge by enhancing a state-of-the-art ocean general
92 circulation model (Parallel Ocean Program version 2, POP2) with the capability of simulating
93 $\delta^{18}O_w$, and conducting a first three-dimensional, isotope-enabled, transient ocean simulation with
94 realistic geometry and forcing conditions.
95 We first implemented an oxygen isotope module in POP2 (iPOP2), where $\delta^{18}O_w$ is forced
96 by the isotopic fluxes at the ocean surface and passively transported in the ocean interior, and then
97 validated iPOP2 under present-day climate conditions. We next forced iPOP2 with $\delta^{18}O_w$ at 0‰
98 under Last Glacial Maximum (LGM, ~22 ka) climate conditions (iLGMspin), with $\delta^{18}O$

composition of hydrological variables (precipitation, evaporation, and river runoffs) constructed based on an isotope-enabled atmospheric model (18) under LGM conditions. We stopped iLGMspin after 4,000 years when $\delta^{18}O_w$ reached a global volume-mean value of 1.05‰, within the uncertainties of the reconstructed LGM value of 1.0±0.1‰ (19), but before it reached full equilibrium.

Starting from the LGM state at 22 ka, we performed a transient simulation (iPOP2-TRACE) to the late Bølling-Allerød (B-A) Interstadial at 13 ka under monthly varying surface boundary conditions, which were taken from a fully coupled climate simulation TRACE21. TRACE21 is a transient simulation of the last deglaciation using the CCSM3 climate model with realistic geometry and forcing conditions, including changes in insolation, greenhouse gases, continental ice sheets, and meltwater (Fig. 1*A*, Table S1). Previous work has shown that the simulation successfully reproduces many observed features of the deglacial climate (4, 13, 20). In this way, the physical ocean environment of iPOP2-TRACE evolved in a similar way to TRACE21 (Fig. S3). The $\delta^{18}O$ value of meltwater was prescribed as −31‰ in the Northern Hemisphere beginning 19 ka and −38‰ in the Southern Hemisphere beginning 14.35 ka. Details of the implementation and validation of the tracer module, as well as the LGM spin-up and the iPOP2-TRACE simulations are given in the *Supporting Information* and Zhang (21). A key feature of iPOP2-TRACE is its capability of quantifying the contribution of local water temperature to $\delta^{18}O_c$ (22), thus providing a dynamic framework for understanding the mechanisms responsible for the evolution of $\delta^{18}O_c$ during the last deglaciation.

Model Ocean Evolution and Isotopic Model-Data Comparison

In our model, strong AABW forms during the LGM due to brine rejection associated with sea-ice expansion around Antarctica. The strong AABW formation, along with a vigorous counterclockwise abyssal overturning, causes the boundary between NADW and AABW to be shallower during the LGM (2.7 km) compared to today (3.3 km), with AABW filling most of the deep Atlantic (Fig. 2), consistent with paleonutrient tracers (23). During HS1, freshwater forcing nearly shuts down NADW transport (from 15 Sv to 2.5 Sv, Sv $\equiv 10^6$ m^3 s^{-1}; Fig. 1*B*). In contrast, AABW transport only decreases by 20% (Fig. 1*C*) due to surface warming and reduced brine rejection associated with significant sea-ice retreat in the Southern Ocean (SO) (Fig. S4), similar to other model simulations which show little AABW response to a collapsed AMOC (24). The relative changes of water-mass volumes lead to further deep-ocean occupation by AABW and a shoaling of the NADW-AABW boundary by ~700 m (Fig. 2*C*). The decrease in ventilation of the intermediate and deep North Atlantic (NA) by northern and southern sources results in it becoming largely isolated, with only slow renewal by AABW through the abyssal overturning. These simulated changes in NA ocean circulation are consistent with (i) various proxies that identify a reduced AMOC intensity (3, 25, 26) (e.g., Fig. 1*B*), (ii) the increased radiocarbon benthic-planktonic age offset at Iberian Margin (27) as a proxy for older apparent ventilation ages (Fig. 1*D*, radiocarbon simulation is given in the *Supporting Information*), and (iii) benthic $\delta^{13}C$ proxies showing accumulation of respired carbon in the intermediate and deep NA (24). We suggest that ventilation of the deep SO increased during HS1 (5) because of greater air-sea interactions and release of low-^{14}C CO_2 associated with sea-ice retreat (28, 29).

The simulated ocean circulation successfully reproduces the basin-wide pattern of the observed $\delta^{18}O_c$ changes across the intermediate and deep Atlantic between late HS1 and the LGM as constrained by 31 high-resolution, independently dated benthic $\delta^{18}O_c$ records (Fig. 3; with

145 correlation r = 0.82, Fig. S5). In particular, the model and data are characterized by greatest
146 changes in the upper NA and little change in the deep SO. The modeled $\delta^{18}O_c$ also captures several
147 other observed $\delta^{18}O_c$ changes, such as in the mid-depth NA (8) and near the Brazil Margin (30)
148 (*Supporting Information*), although it tends to overestimate the amplitude of $\delta^{18}O_c$ changes at
149 intermediate depths (Fig. S5 and S8), the causes and impact of which we discuss later.

150 To examine the regional phasing of the deep $\delta^{18}O_c$ response, we compared our simulation
151 results with two well-dated, high-resolution benthic $\delta^{18}O_c$ records, one from the Iberian Margin in
152 the NA (MD99-2334K, 37.8°N, 3146 m) (6, 31) and the other in the Atlantic sector of the SO
153 (MD07-3076Q, 44.2°S, 3770 m) (5, 8). These cores also have bottom-water temperature
154 reconstructions (6, 32) which, although having lower resolution and higher analytical uncertainty
155 than the $\delta^{18}O_c$ data, allows for a general comparison. In both the model and the records (Fig. 1*E*),
156 $\delta^{18}O_c$ shows a gradual post-glacial increase from 22 ka to 19 ka, which is likely caused by the
157 increase of $\delta^{18}O_w$ (Fig. 1*F*), since the water temperature remains unchanged during this period
158 (Fig. 1*G*). The ocean reached its maximum $\delta^{18}O_w$ enrichment when ice sheets reached their
159 maximum extent at ~22 ka. The enrichment was not simultaneous throughout the global ocean,
160 however, but peaked sequentially from the surface to deep and across different ocean basins well
161 after 22 ka (8, 33) (Fig. S9) due to the long overturning timescale of the ocean, from ~1,500 yr in
162 the Atlantic to more than 3,000 yr in the Pacific.

163 From 19 ka to 16 ka, the modeled $\delta^{18}O_c$ captures the observed earlier and greater $\delta^{18}O_c$
164 decrease in the NA (~0.6‰) than in the SO (~0.2‰). The cause of this earlier $\delta^{18}O_c$ decrease at
165 deep NA core sites during HS1 is widely debated. One "southern-source" hypothesis suggests that
166 reduced formation of NADW during HS1 enhanced the formation and northward expansion of
167 southern-sourced low-$\delta^{18}O$, low-$\delta^{13}C$ AABW (6, 7). An alternative "northern-source" hypothesis

168 argues that during HS1, the NA was influenced by overflows of brine-generated deepwater formed
169 by sea-ice expansion in the Nordic Seas, with the low $\delta^{18}O$ signal reflecting meltwater transferred
170 to depth during brine formation (8–10) and the low $\delta^{13}C$ values reflecting suppressed air-sea gas
171 exchange (8). Temperature may also have played a role in affecting the deglacial $\delta^{18}O_c$ signal, and
172 increasing evidence of mid-depth warming in the NA during HS1 (20, 34, 35) implies this warming
173 should be taken into account to explain the mid-depth $\delta^{18}O_c$ decrease. In the deep Atlantic,
174 however, a lack of high-resolution temperature reconstructions leads to large uncertainties in the
175 sign and magnitude of temperature change in each hemisphere (7, 36), and in turn its contribution
176 to deep $\delta^{18}O_c$.

177 In this context, our model results indicate that the observed lead of the deglacial $\delta^{18}O_c$
178 decrease in the deep NA over the SO is due to asynchronous warming of deepwater rather than to
179 a change in the contributions of NADW or AABW, or their $\delta^{18}O_w$ values. During HS1, the
180 simulated $\delta^{18}O_w$ component shows nearly coherent decreases at both core sites (Fig. 1*F*). These
181 depletions at depth are caused primarily by the transfer of ^{18}O-depleted surface meltwater, with a
182 change of surface precipitation and evaporation playing a minor role (Fig. S10, *Supporting*
183 *Information*). Although the decrease of NA $\delta^{18}O_w$ is slightly greater since the site is geographically
184 closer to the meltwater source, the difference is nearly indistinguishable and cannot explain the
185 much larger differences seen in the records. In contrast, the temperature component exhibits strong
186 asynchrony, with the deep ocean below 3000 m warming by ~1.4°C in the north but experiencing
187 little change in the south, roughly consistent with Mg/Ca temperature reconstructions (6, 32) (Fig.
188 1*G*). The warming in the north causes $\delta^{18}O_c$ to decrease by ~0.35‰, thus explaining most of the
189 0.4‰ difference between the two records.

The relative contributions of $\delta^{18}O_w$ and temperature can be seen more clearly in the basin-wide responses. In response to the input of ^{18}O-depleted freshwater during HS1, $\delta^{18}O_w$ decreases over the entire basin relative to its LGM values (Fig. 4*E*), similar to the salinity response. A considerable portion of the ^{18}O-depleted freshwater is trapped in the upper NA and within the Labrador Sea and the Nordic Seas (Fig. 4*C*). An anomalous tongue of modest size (~ −0.1‰) extends downward and southward along the lower limb of the diminishing glacial AMOC during the transition to HS1, and further disperses into the whole ocean through residual circulation and mixing (Fig. 4*E*). This $\delta^{18}O_w$ response in the Atlantic basin is similar to what has previously been simulated in a model of intermediate complexity (12). In contrast, the temperature field shows a bipolar seesaw response at the surface and basin-wide warming in the subsurface (Fig. 4*F*), consistent with observations (20, 34, 35). Notably, the warming occurs all the way to the abyss in the NA but not in the SO, generating a deep meridional temperature gradient that accounts for the $\delta^{18}O_c$ gradient across the deep Atlantic.

Mechanisms of Tracer Evolution during HS1

The impact of circulation on $\delta^{18}O_w$ distribution. We conducted two sensitivity experiments to separate the circulation effect from the boundary effect on $\delta^{18}O_w$ distribution. One experiment (iPOP2-19ka) simulated $\delta^{18}O_w$ with transient surface forcing from 19 ka to 16 ka, but with the circulation held at the 19-ka level. This was achieved by looping the boundary conditions of 20–19 ka of TRACE21 but applying the transient $\delta^{18}O_w$ surface fluxes taken from iPOP2-TRACE. The other experiment (iPOP2-0ka) was similar to iPOP2-19ka, but with a modern circulation pattern forced by CORE-II inter-annually varying atmospheric data sets (37).

When the circulation is held at its 19-ka level, the low-$\delta^{18}O$ signal is no longer able to accumulate in the upper NA during HS1 as in iPOP2-TRACE (Fig. 4*E*), but is well distributed in the whole Atlantic (Fig. 4*G*) and extends to the Pacific and Indian oceans. This suggests that the strong reduction in NADW formation and associated overflows is the direct cause of the trapped ^{18}O-depleted water in iPOP2-TRACE. We also note that the tongue of southward expansion of the ^{18}O-depleted water is confined to above 3000 m in iPOP2-19ka (Fig. 4*G*), even with a strong and fully functional AMOC. This is because NADW is confined above the thick abyssal layer of AABW (Fig. 2*B*). In contrast, the expansion of the low-$\delta^{18}O$ tongue in iPOP2-0ka reaches deeper in the NA with more tilted contours (Fig. 4*H*), consistent with the modern AMOC pattern (Fig. 2*A*).

Physical processes at the two core sites. We conducted a tracer budget analysis to identify the specific physical processes as responsible for the different $\delta^{18}O_w$ and temperature responses during HS1 (*Supporting Information*). During the LGM, $\delta^{18}O_w$ is increasingly depleted with depth in the northern NA, while during HS1, this vertical gradient reverses due to the input of highly ^{18}O-depleted freshwater at the surface (Fig. 5*A*). The $\delta^{18}O_w$ budget at 3100 m shows a regime shift during HS1 to a dominant balance between two vertical processes, namely vertical mixing and vertical advection, and an over-90% decrease of the horizontal advective fluxes (Fig. 5*B*). The surface low-$\delta^{18}O$ signal weakens with depth, because vertical mixing takes a long time to transfer the signal from the surface down to 3100 m in the absence of deep convection. The deep NA therefore experiences little $\delta^{18}O_w$ change even though it is geographically close to the freshwater input. In contrast, the $\delta^{18}O_w$ in the SO has a mild, vertically uniform transition (Fig. 5*C*), and the

235 regime shift of the $\delta^{18}O_w$ budget found in the northern NA does not occur in the deep SO (Fig.
236 5*D*).

237 Unlike the passive response of $\delta^{18}O_w$, the temperature response involves dynamic
238 processes that cause significant warming at depth. The heat budget in the northern NA at 3100 m
239 experiences a regime shift similar to that of the $\delta^{18}O_w$ budget, and it is the enhanced downward
240 heat flux by vertical mixing that overwhelms an enhanced upwelling of cold water (i.e., vertical
241 advection) and heats the deep NA (Fig. 5*F*). The key to understanding why vertical mixing can
242 effectively change the temperature field but not the $\delta^{18}O_w$ field lies with the vertical structure of
243 the different signals. In response to the onset of freshwater forcing at 19 ka, the mid-depth warming
244 occurs first at 2000 m depth (Fig. 5*E*). This depth corresponds to the winter-season maximum
245 mixed-layer depth in the NA at the LGM (Fig. S12), indicating the deepest layer that deep
246 convection can reach. During the LGM, strong deep convection occurs in the northern NA rather
247 than mostly in the Nordic Seas as during present-day. It maintains colder temperatures at 50°N
248 above 2000 m depth than those of other Atlantic regions at the same depths (Fig. 4*B*) by mixing
249 cold water that is chilled by intense atmospheric cooling downwards and warm mid-depth water
250 upwards. At 19 ka, winter-season deep convection shallows from 2000 m to 1500 m and allows
251 heat to accumulate within this layer. Therefore, the mid-depth heat can be more effectively
252 transported by vertical mixing from 2000 m downward, compared with the low-$\delta^{18}O$ signal which
253 originates at surface.

254 In contrast to the NA, the SO temperatures change little at depth, despite warming in the
255 upper layers due to reduced northward oceanic heat transport. Close to the deep SO mean
256 temperature front (~40°S), where isotherms are strongly tilted, the heat budget is balanced between
257 a cold eddy heat transport (a major component in horizontal mixing) and a warm tendency of other

processes (i.e., the eddy–mean advection balance; Fig. 5*H*). Reduced AABW formation and associated mass transport in the abyssal overturning decreases the northward advection of cold AABW, tending to induce warming at depth. However, the eddy–mean advection balance is so dominant (38) that this warming tendency is largely offset by the enhanced cooling from eddy transport, so that SO warming is confined to the upper ocean (Fig. 5*G*).

Further assessment of model and data uncertainties. Although our model results provide a self-consistent physical mechanism for the observed phasing of $\delta^{18}O_c$ records in the deep Atlantic, we identify additional work that is needed to further test this hypothesis. One issue is related to our model simulation that tends to overestimate the LGM-to-HS1 $\delta^{18}O_c$ decrease at intermediate depths, which could be due to some combination of excessive local $\delta^{18}O_w$ decrease and excessive local warming. The excessive $\delta^{18}O_w$ decrease may be caused by evenly distributing freshwater forcing over the area of 50–70°N in the Atlantic, which could transport excessive low-^{18}O water into mid-depth. Observations indicate freshwater is more likely distributed along a narrow region off the coast (39) and along iceberg pathways. Moreover, assessing whether the model produces excessive mid-depth warming is difficult due to the lack of high-resolution, low-uncertainty temperature reconstructions in the mid-depth NA. Similarly, further testing asynchronous deep warming will require additional temperature reconstructions, given the uncertainties of the temperature reconstructions at MD99-2334K and MD07-3076Q, and that the LGM mean value at the latter site is 3°C higher than the model.

Discussion and Conclusions

Our study suggests a scenario of nearly collapsed NADW and mildly weakened AABW during HS1, consistent with available benthic $\delta^{18}O_c$ constraints of greatest deglacial decreases in the upper NA and little change in the deep SO across the Atlantic basin and, especially, of an earlier $\delta^{18}O_c$ decrease in deep NA records than in the deep SO. We identify asynchronous warming between the deep NA and SO during times of reduced AMOC as the reason for the early decrease of the deep NA $\delta^{18}O_c$. We suggest a dynamic process to explain the early warming in the deep NA, which emphasizes mid-depth warming due to a shoaling of deep convection and enhanced downward heat flux via vertical mixing that transfers heat from intermediate depths to the deep ocean.

Our proposed warming mechanism has two major differences from previous studies. First, some previous studies (e.g., "deep-decoupling oscillation") suggested that the NA mid-depth warming originated from diffusion of tropical ocean heat across the main thermocline and transported northward (20, 35, 40–42). If the heat were from the tropics, the NA isotherms would deepen gradually from the depth of the main thermocline (~300–500 m) to lower layers and would probably lag the freshwater event by decades or even longer (40). However, our model suggests the mid-depth warming occurs first at 2000 m and immediately with the freshwater forcing onset. We thus argue that the northern NA mid-depth warming is caused largely by the shoaling of winter-season deep-convection depth. Additional supporting evidence is that another rapid mid-depth warming occurs at 17.4–17.2 ka (Fig. 5*E*), when isotherms between 400–1300 m experience a sudden deepening, corresponding to a second rapid shoaling of the deep-convection depth from 1300 m to 400 m (Fig. S12*D*) in response to the increased rate of freshwater forcing (Fig. 1*A*). This physical process may be used to explain the large and abrupt warming at 2000 m depth during HS1 observed in deep-sea corals in the western NA as well as the contemporaneous shift to more

303 ^{14}C-depleted waters (34) (Fig. S13), although the observed abrupt warming and aging occurred
304 later than in the model.

305 The second notable difference between our mechanism and the "deep decoupling
306 oscillation" is that the latter suggests that the reduced AMOC causes a diffusive warming of the
307 deep ocean by a reduction in the upwelling of cold water (40, 43). However, our heat-budget
308 analysis shows an enhanced cooling effect from the upwelling (Fig. 5*E*). The upwelling velocity
309 (w) indeed decreases, but the increase of the vertical temperature gradient ($\partial T/\partial z$) is so large that
310 it overwhelms the velocity effect and causes the vertical advective cooling ($w\partial T/\partial z$) to increase
311 (Fig. S14). Both the vertical mixing and vertical advection are actually enhanced by this increased
312 $\partial T/\partial z$, with the former enhanced more. We thus conclude that it is the enhanced downward heat
313 transport via vertical mixing, rather than the reduced upwelling of cold water, that effectively heats
314 the deep NA.

Acknowledgements

We thank B. Otto-Bliesner for her support throughout the work; J. Gottschalk, S. Gu, J. Zhu, and A. Hu for helpful discussions; G. Danabasoglu, D. Bailey, and S. Bates for modeling technical assistance; and J. Roberts, D. Lund, L. Skinner, and S. Weldeab for providing data. This work is supported by the U.S. NSF P2C2 projects (1401778 and 1401802) and OCE projects (1600080 and 1566432), China NSFC 41630527, and the Wisconsin Alumni Research Foundation. Computing resources were provided by the Climate Simulation Laboratory at NCAR's Computational and Information Systems Laboratory (CISL), sponsored by U.S. NSF and other agencies.

References

1. Broecker WS (1998) Paleocean circulation during the Last Deglaciation: A bipolar seesaw? *Paleoceanography* 13(2):119–121.
2. Roberts NL, Piotrowski AM, McManus JF, Keigwin LD (2010) Synchronous deglacial overturning and water mass source changes. *Science* 327(5961):75–8.
3. McManus JF, Francois R, Gherardi J-M, Keigwin LD, Brown-Leger S (2004) Collapse and rapid resumption of Atlantic meridional circulation linked to deglacial climate changes. *Nature* 428(6985):834–7.
4. Shakun JD, et al. (2012) Global warming preceded by increasing carbon dioxide concentrations during the last deglaciation. *Nature* 484(7392):49–54.
5. Skinner LC, Fallon S, Waelbroeck C, Michel E, Barker S (2010) Ventilation of the deep Southern Ocean and deglacial CO_2 rise. *Science* 328(5982):1147–1151.
6. Skinner LC, Shackleton NJ, Elderfield H (2003) Millennial-scale variability of deep-water temperature and $\delta^{18}O_{dw}$ indicating deep-water source variations in the Northeast Atlantic, 0-34 cal. ka BP. *Geochem, Geophys Geosyst* 4(12). doi:10.1029/2003GC000585.
7. Skinner LC, Shackleton NJ (2006) Deconstructing Terminations I and II: revisiting the glacioeustatic paradigm based on deep-water temperature estimates. *Quat Sci Rev* 25(23–24):3312–3321.
8. Waelbroeck C, et al. (2011) The timing of deglacial circulation changes in the Atlantic. *Paleoceanography* 26(3):PA3213.
9. Meland MY, Dokken TM, Jansen E, Hevrøy K (2008) Water mass properties and exchange between the Nordic seas and the northern North Atlantic during the period 23-6 ka: Benthic oxygen isotopic evidence. *Paleoceanography* 23(1):PA1210.
10. Thornalley DJR, Elderfield H, McCave IN (2010) Intermediate and deep water paleoceanography of the northern North Atlantic over the past 21,000 years. *Paleoceanography* 25(1):PA1211.
11. Lea DW (2014) Elemental and isotopic proxies of past ocean temperatures. *Treatise on Geochemistry*, eds Holland HD, Turekian KK (Elsevier), pp 373–397. 2nd Ed.
12. Ganopolski A, Roche DM (2009) On the nature of lead–lag relationships during glacial–interglacial climate transitions. *Quat Sci Rev* 28(27–28):3361–3378.
13. Liu Z, et al. (2009) Transient simulation of last deglaciation with a new mechanism for Bølling-Allerød warming. *Science* 325(5938):310–314.
14. Smith RS, Gregory J (2012) The last glacial cycle: transient simulations with an AOGCM. *Clim Dyn* 38(7–8):1545–1559.
15. Friedrich T, Timmermann A (2012) Millennial-scale glacial meltwater pulses and their effect on the spatiotemporal benthic $\delta^{18}O$ variability. *Paleoceanography* 27(3):PA3215.
16. Roche DM, Paillard D, Caley T, Waelbroeck C (2014) LGM hosing approach to Heinrich Event 1: results and perspectives from data–model integration using water isotopes. *Quat Sci Rev* 106:247–261.
17. Bagniewski W, Meissner KJ, Menviel L, Brennan CE (2015) Quantification of factors impacting seawater and calcite $\delta^{18}O$ during Heinrich Stadials 1 and 4. *Paleoceanography* 30(7):895–911.
18. Liu Z, et al. (2014) Chinese cave records and the East Asia Summer Monsoon. *Quat Sci Rev* 83:115–128.
19. Schrag DP, et al. (2002) The oxygen isotopic composition of seawater during the Last Glacial Maximum. *Quat Sci Rev* 21(1–3):331–342.

20. Marcott SA, et al. (2011) Ice-shelf collapse from subsurface warming as a trigger for Heinrich events. *Proc Natl Acad Sci USA* 108(33):13415–9.
21. Zhang J (2016) Understanding the deglacial evolution of deep Atlantic water masses in an isotope-enabled ocean model. Dissertation (University of Wisconsin-Madison).
22. Marchitto TM, et al. (2014) Improved oxygen isotope temperature calibrations for cosmopolitan benthic foraminifera. *Geochim Cosmochim Acta* 130:1–11.
23. Curry WB, Oppo DW (2005) Glacial water mass geometry and the distribution of $\delta^{13}C$ of ΣCO_2 in the western Atlantic Ocean. *Paleoceanography* 20(1):PA1017.
24. Schmittner A, Lund DC (2015) Early deglacial Atlantic overturning decline and its role in atmospheric CO_2 rise inferred from carbon isotopes ($\delta^{13}C$). *Clim Past* 11(2):135–152.
25. Clark PU, et al. (2012) Global climate evolution during the last deglaciation. *Proc Natl Acad Sci USA* 109(19):E1134–E1142.
26. Buizert C, et al. (2014) Greenland temperature response to climate forcing during the last deglaciation. *Science* 345(6201):1177–1180.
27. Skinner LC, Waelbroeck C, Scrivner AE, Fallon SJ (2014) Radiocarbon evidence for alternating northern and southern sources of ventilation of the deep Atlantic carbon pool during the last deglaciation. *Proc Natl Acad Sci USA* 111(15):5480–4.
28. Keeling RF, Stephens BB (2001) Antarctic sea ice and the control of Pleistocene climate instability. *Paleoceanography* 16(1):112–131.
29. Sigman DM, Hain MP, Haug GH (2010) The polar ocean and glacial cycles in atmospheric CO_2 concentration. *Nature* 466(7302):47–55.
30. Lund DC, Tessin AC, Hoffman JL, Schmittner A (2015) Southwest Atlantic water mass evolution during the last deglaciation. *Paleoceanography* 30(5):477–494.
31. Skinner LC, Shackleton NJ (2004) Rapid transient changes in northeast Atlantic deep water ventilation age across Termination I. *Paleoceanography* 19(2):PA2005.
32. Roberts J, et al. (2016) Evolution of South Atlantic density and chemical stratification across the last deglaciation. *Proc Natl Acad Sci USA* 113(3):514–519.
33. Stern J V., Lisiecki LE (2014) Termination 1 timing in radiocarbon-dated regional benthic $\delta^{18}O$ stacks. *Paleoceanography* 29(12):1127–1142.
34. Thiagarajan N, Subhas A V, Southon JR, Eiler JM, Adkins JF (2014) Abrupt pre-Bølling-Allerød warming and circulation changes in the deep ocean. *Nature* 511(7507):75–8.
35. Weldeab S, Friedrich T, Timmermann A, Schneider RR (2016) Strong middepth warming and weak radiocarbon imprints in the equatorial Atlantic during Heinrich 1 and Younger Dryas. *Paleoceanography* 31:1–13.
36. Oppo DW, Curry WB, McManus JF (2015) What do benthic $\delta^{13}C$ and $\delta^{18}O$ data tell us about Atlantic circulation during Heinrich Stadial 1? *Paleoceanography* 30(4):353–368.
37. Griffies SM, et al. (2012) *Datasets and protocol for the CLIVAR WGOMD Coordinated Ocean-sea ice Reference Experiments (COREs)*.
38. Henning CC, Vallis GK (2005) The Effects of Mesoscale Eddies on the Stratification and Transport of an Ocean with a Circumpolar Channel. *J Phys Oceanogr* 35(5):880–896.
39. Condron A, Winsor P (2012) Meltwater routing and the Younger Dryas. *Proc Natl Acad Sci USA* 109(49):19928–19933.
40. Winton M, Sarachik ES (1993) Thermohaline Oscillations Induced by Strong Steady Salinity Forcing of Ocean General Circulation Models. *J Phys Oceanogr* 23(7):1389–1410.
41. Olsen SM, Shaffer G, Bjerrum CJ (2005) Ocean oxygen isotope constraints on

mechanisms for millennial-scale climate variability. *Paleoceanography* 20(1):1–19.
42. Mignot J, Ganopolski A, Levermann A (2007) Atlantic subsurface temperatures: Response to a shutdown of the overturning circulation and consequences for its recovery. *J Clim* 20(19):4884–4898.
43. Palter JB, et al. (2014) The deep ocean buoyancy budget and its temporal variability. *J Clim* 27(2):551–573.
44. Jahn A, et al. (2015) Carbon isotopes in the ocean model of the Community Earth System Model (CESM1). *Geosci Model Dev* 8(8):2419–2434.
45. Lambeck K, Rouby H, Purcell A, Sun Y, Sambridge M (2014) Sea level and global ice volumes from the Last Glacial Maximum to the Holocene. *Proc Natl Acad Sci USA* 111(43):15296–15303.

427 **Figures**

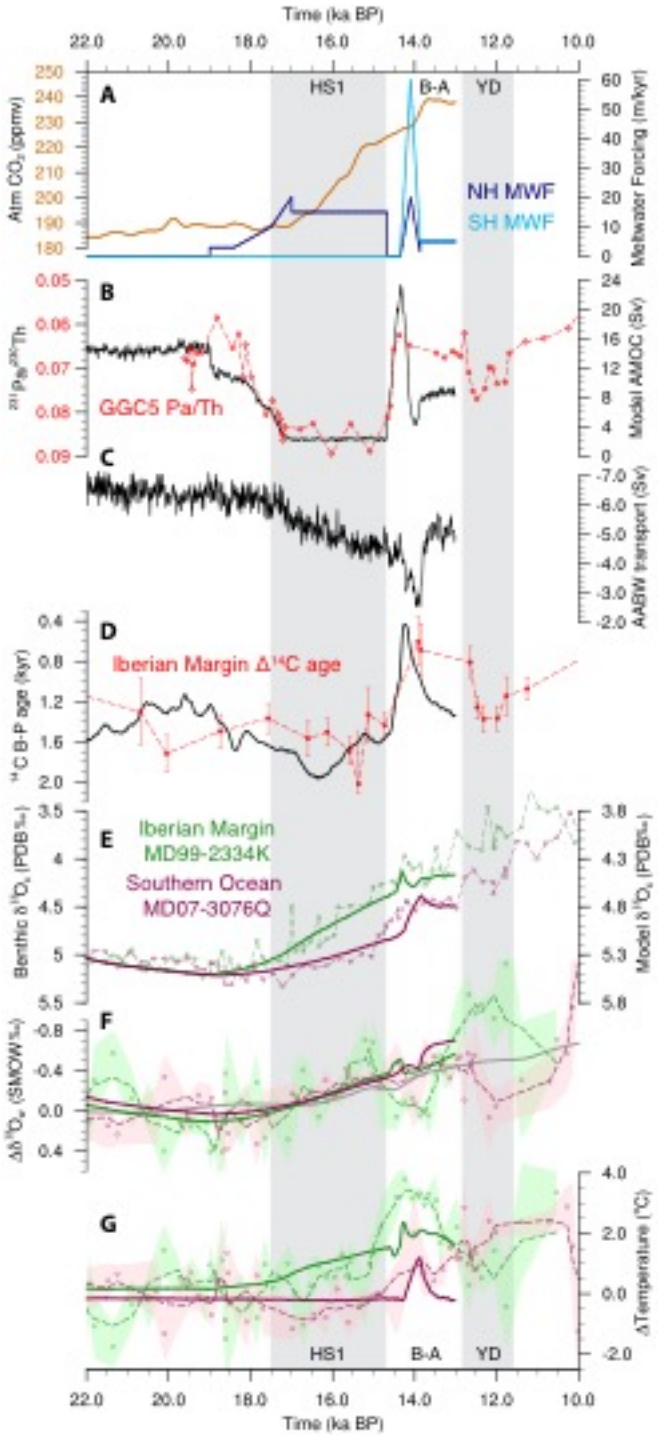

428

429 **Figure 1.**

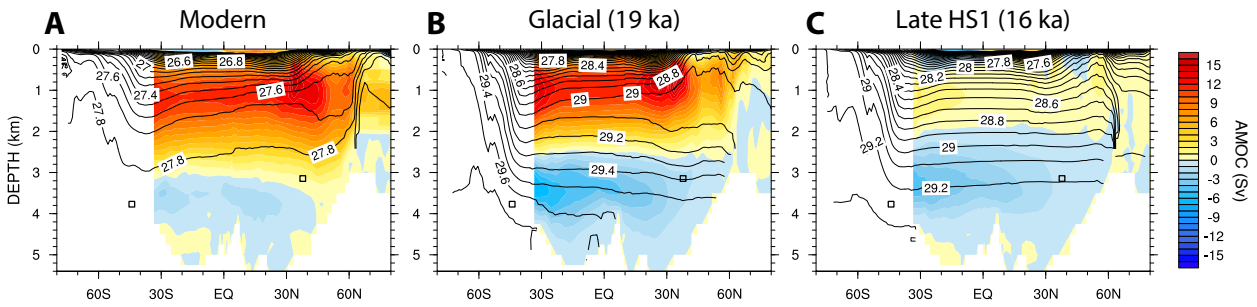
A
Modern
B
Glacial (19 ka)
C
Late HS1 (16 ka)
DEPTH (km)
0
1
2
3
4
5
60S
30S
EQ
30N
60N
26.6
26.8
27.6
27.4
27.8
28.4
28.8
29
29.2
29.4
29.6
28
28.2
28.6
28.8
29
29.2
15
12
9
6
3
0
-3
-6
-9
-12
-15
AMOC (Sv)

Figure 2.

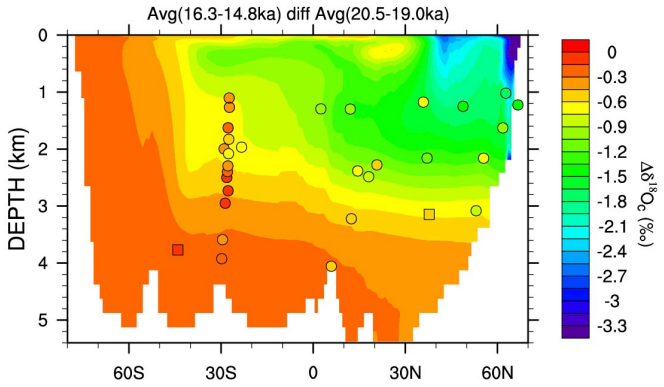

433

434 **Figure 3.**

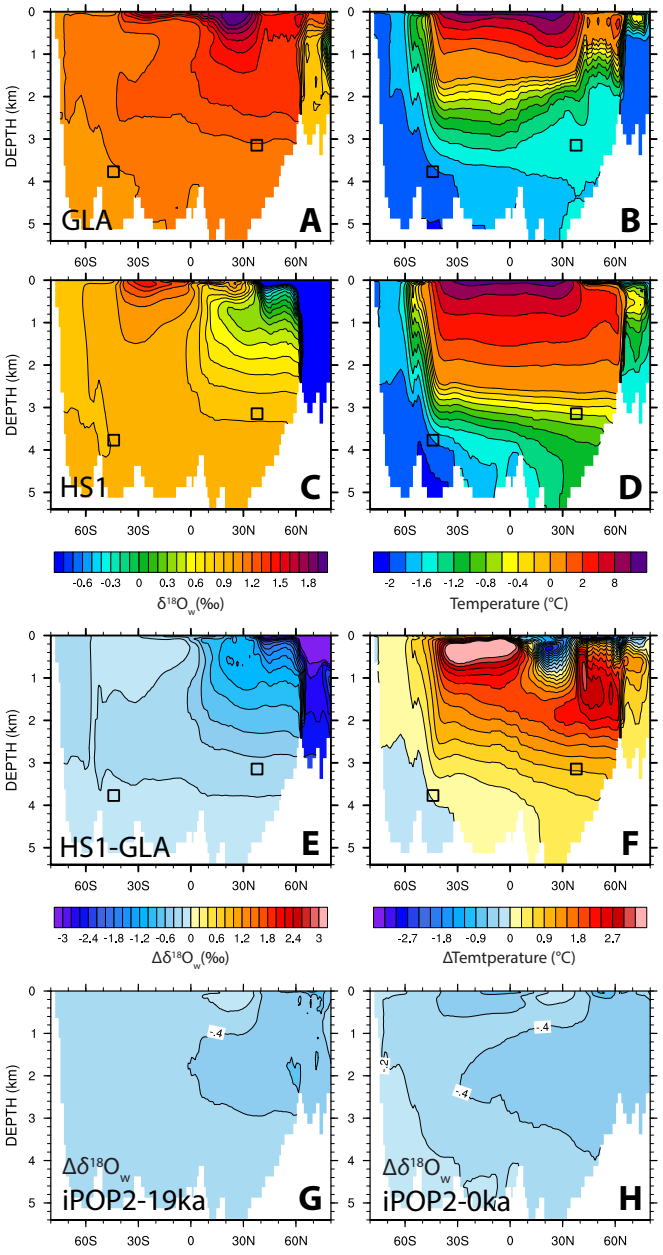

435

436 **Figure 4.**

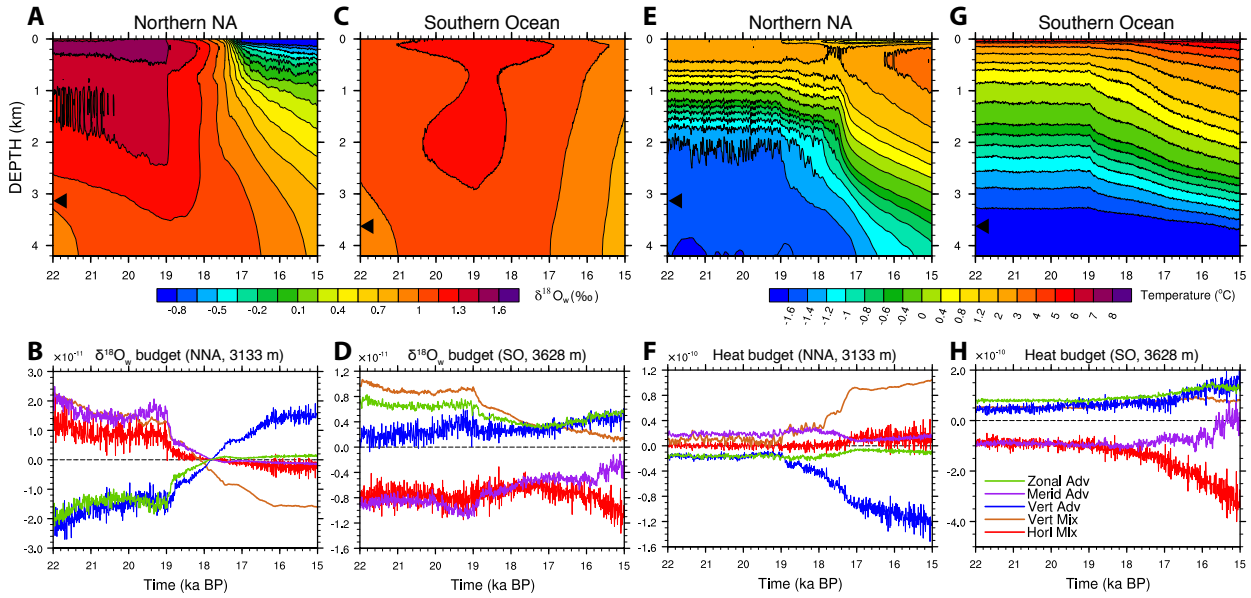

437

438 **Figure 5.**

Figure legends

Fig. 1. Model deglacial signals compare with proxies. (*A*) Atmospheric CO_2 concentration (orange) and meltwater fluxes of the Northern (navy) and Southern (blue) Hemispheres (Table S1) applied in TRACE21 (13). (*B*) Pa/Th ratio at Bermuda [GGC5 (3)] as a proxy for the strength of AMOC and model maximum AMOC transport (below 500 m). (*C*) Model AABW transport in the Atlantic basin (the minimum AMOC transport below 2000 m). The negative values indicate counterclockwise circulation. (*D*) ^{14}C benthic-planktonic (B-P) age offset at Iberian Margin [MD99-2334K (27)] and model abiotic ^{14}C B-P age (44) at this site. (*E*) Benthic $\delta^{18}O_c$ at Iberian Margin [MD99-2334K (6, 31), green] and Southern Ocean [MD07-3076Q (5, 8), pink], and the corresponding model $\delta^{18}O_c$. (*F*) Reconstructed deepwater $\delta^{18}O_w$ anomalies (respective LGM mean was subtracted) at MD99-2334K (6) and MD07-3076Q (32) compared with the corresponding model $\delta^{18}O_w$ anomalies. Open circles represent the raw data; shades represent the estimated uncertainty based on average deviation of adjacent measurements; and dashed lines represent 3-point smoothing (6). Global mean $\delta^{18}O_w$ anomaly (gray) is converted from ice-volume equivalent sea level (45) by 1.05‰/145 m. (*G*) Same as *F*, but for deepwater temperature anomalies based on Mg/Ca measurements (6, 32). All dashed lines indicate proxies, and solid lines indicate model results. HS1, Heinrich Stadial 1; B-A, Bølling-Allerød; YD, Younger Dryas.

Fig. 2. Atlantic total meridional overturning circulation at modern (*A*), glacial at 19 ka (*B*), and late HS1 at 16 ka (*C*). Total circulation, also known as residual circulation, is the sum of the Eulerian-mean circulation and the circulation caused by mesoscale eddies (submesoscale eddies are ignored since they are small and concentrated at surface layers), and is directly related to tracer

462 transport. The Atlantic zonal-mean potential densities (σ_θ) of each period are overlaid in black
463 contours, with interval of 0.1 kg m^{-3}. Squares indicate the two cores sites of Fig. 1*E*.
464
465 **Fig. 3.** Deglacial benthic $\delta^{18}O_c$ changes in the Atlantic. Contours are zonally averaged Atlantic
466 $\delta^{18}O_c$ changes between late HS1 (16.3–14.8 ka mean) and glacial (20.5–19.0 ka mean) periods in
467 the model. Circles and squares are reconstructed benthic $\delta^{18}O_c$ changes at 31 independently-dated
468 core cites (Table S2) between these two periods. Squares indicate the two cores sites of Fig. 1*E*.
469
470 **Fig. 4.** (*A* to *F*) Atlantic zonally averaged $\delta^{18}O_w$ (left column) and potential temperature (right
471 column). From top to bottom panels are variables at 19 ka (*A* and *B*), 16 ka (*C* and *D*), and their
472 differences (*E* and *F*). Squares indicate the two core sites of Fig. 1*E*. Note the colorbar for *B* and
473 *D* is non-linear. The deep North Atlantic core site experiences reversed $\delta^{18}O_w$ vertical gradient and
474 enlarged temperature vertical gradient from 19 ka to 16 ka. (*G* and *H*) The $\delta^{18}O_w$ differences
475 between 16 ka and 19 ka of the two sensitivity experiments iPOP2-19ka and iPOP2-0ka, sharing
476 the same colorbar with *E*.
477
478 **Fig. 5.** Hovmöller diagrams of tracer vertical profiles (upper panel) and tracer budget analysis
479 (lower panel) for the 22–15 ka time interval. (*A*) Hovmöller diagrams of area averaged $\delta^{18}O_w$
480 vertical profiles in the northern NA (>30°N). Black triangles indicate the depth at which the $\delta^{18}O_w$
481 budget analysis is performed. (*B*) Time series of area averaged $\delta^{18}O_w$ budget terms (in 10^{-11} ‰ s^{-1})
482 in this region at 3133 m (corresponding to the MD99-2334K core depth), with positive values
483 indicating $\delta^{18}O_w$ gain. The zonal (green), meridional (purple), and vertical (blue) mean advective
484 fluxes as well as the vertical (brown) and horizontal (red) mixing are plotted. (*C* and *D*) Same as

485 *A* and *B*, but for the 36–46°S South Atlantic, and the budget analysis is performed at 3628 m
486 (corresponding to the MD07-3076Q core depth). (*E* to *H*) Same as *A* to *D*, but for temperature
487 profiles and heat budget terms (in 10^{-10} °C s^{-1}). Note the colorbar for *E* and *G* is non-linear.